

Humanoid Whole-Body Badminton via Multi-Stage Reinforcement Learning

Chenhao Liu*, Leyun Jiang[†], Yibo Wang[†], Kairan Yao, Jinchun Fu and Xiaoyu Ren
Beijing Phybot Technology Co., Ltd, Beijing, China 100089
Email: liuchenhao@phybot.cn

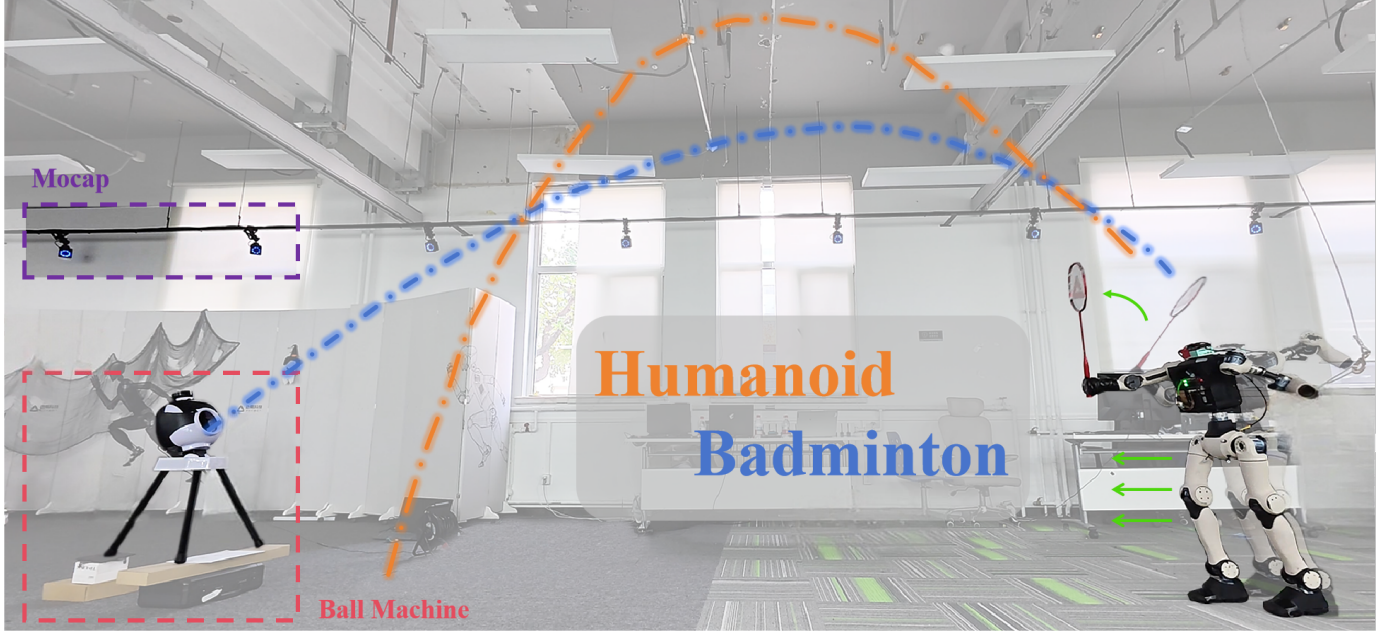


Fig. 1: **Real-world humanoid badminton.** A fully autonomous humanoid returns machine-fed shuttles in a motion-capture arena; overlaid arcs show an incoming (blue) and returned (orange) trajectory. Project Page: humanoid-badminton.github.io.

Abstract—Humanoid robots have demonstrated strong capabilities for interacting with static scenes across locomotion, manipulation, and more challenging loco-manipulation tasks. Yet the real world is dynamic, and quasi-static interactions are insufficient to cope with diverse environmental conditions. As a step toward more dynamic interaction scenarios, we present a reinforcement-learning-based training pipeline that produces a unified whole-body controller for humanoid badminton, enabling coordinated lower-body footwork and upper-body striking without motion priors or expert demonstrations. Training follows a three-stage curriculum—first footwork acquisition, then precision-guided racket swing generation, and finally task-focused refinement—yielding motions in which both legs and arms serve the hitting objective. For deployment, we incorporate an Extended Kalman Filter (EKF) to estimate and predict shuttlecock trajectories for target striking. We also introduce a prediction-free variant that dispenses with EKF and explicit trajectory prediction. To validate the framework, we conduct five sets of experiments in both simulation and the real world. In simulation, two robots sustain a rally of 21 consecutive hits. Moreover, the prediction-free variant achieves successful hits with comparable performance relative to the target-known policy. In real-world tests, both prediction and controller modules exhibit high accuracy, and on-court hitting achieves an outgoing shuttle speed up to 19.1 m/s with a mean return landing distance of 4 m. These experimental results show that our proposed training

scheme can deliver highly dynamic while precise goal striking in badminton, and can be adapted to more dynamics-critical domains.

I. INTRODUCTION

Humanoid platforms have been proposed as general-purpose embodied agents for human-compatible skills [1, 2, 3, 4, 5, 6, 7]. Despite rapid progress in locomotion and motion imitation, agile, contact-rich interactions with fast-moving objects under tight reaction windows remain underexplored. Badminton is a particularly ideal testbed: returns require sub-second perception–action loops, precisely timed and oriented racket–shuttle contacts within a large 3D interception volume, and whole-body coordination that blends rapid arm swings with stable and agile leg motions.

Compared with several recent works on robotic table tennis [8, 9, 10, 11], badminton aggravates several difficulties. Aerodynamics are highly uncertain: strong drag and a special “flip” regime make the pre-turning trajectory hard to model; as a result, the seemingly longer flight still yields less usable decision time. Although the racket face is larger, valid hits occur only in brief windows when position, velocity, and orientation

align; swing amplitudes are also much larger, injecting angular momentum that challenges whole-body balance. Critically, footwork and striking must co-evolve: lower-body motion does not merely reposition the base but co-determines hitting accuracy. Our system reaches swing speeds around 5.3 m/s and produces outgoing shuttle speeds up to 19.1 m/s. The serve-to-hit window is 0.8 to 1.0 s; the first 0.36 s is consumed by trajectory prediction, leaving less than 0.6 s for the controller to react.

Humanoids are a natural fit for badminton. Lateral mobility and reach patterns match human-centered rules and court geometry, and established human strategies (e.g., split steps, approach phases, recovery) transfer more directly compared to non-humanoid platforms. Demonstrating badminton on a humanoid, therefore, serves as a stepping stone toward broader, highly dynamic, interactive behaviors in human environments.

Related efforts highlight both promise and gaps. [10] demonstrated humanoid table tennis via a hierarchical planner coupled to a learned whole-body controller and achieved long rallies. Our setting differs in key ways: (i) we do not use reference motions to shape striking; instead, the policy discovers energy-efficient swings purely via reinforcement learning, simplifying implementation, and avoiding excessive style constraints; (ii) The use of “virtual hit plane” reduces striking to a largely 2D problem, whereas badminton demands orientation-aware contacts throughout a 3D space; (iii) badminton’s large-amplitude strokes induce significant whole-body disturbance, requiring balance recovery that table-tennis-scale motions seldom provoke; and (iv) we do not explicitly compute target base positions; instead, the policy only receives the desired interception target and must coordinate the whole-body motion. As for badminton, recent work on a legged-manipulator learns coordinated skills with onboard vision [12]; however, humanoid hardware deployment has remained elusive, and their simulated humanoid badminton policies did not exhibit badminton-style footwork, suggesting missing training signals for lower-body coordination. These gaps motivate a training pipeline that explicitly fosters footwork–strike synergy on humanoids and scales to real hardware.

This paper presents, to our knowledge, the first real-world humanoid robot that plays badminton. We train a unified whole-body controller with a multi-stage reinforcement learning curriculum: (1) footwork acquisition toward target regions with feet-swing time and height regularization; (2) precision-guided arm swing generation with timing and scheduled tightening of position and orientation accuracy; and (3) final refinement that removes numerous locomotion-shaping regularizers to avoid gradient interference and maximize hitting performance. Across all stages, we adopt the shuttlecock simulation of [12] to generate flight trajectories for training. At each rollout, the policy receives a compact target tuple—hit time, intercept position, and target racket orientation—drawn from a pre-generated corpus of about 20k trajectories; intercepts are selected randomly within a 1.5–1.6 m height band, chosen based on the humanoid’s height as a natural overhead hitting zone. Exponential rewards with scheduled tightness transition

behavior from coarse to precise.

The policy observes target hit information as well as proprioception and inferred actions for 21 joints on a 1.28 m custom humanoid. In deployment, the hitting target is obtained online from an EKF that predicts the shuttlecock trajectory. We leverage a Low-level PD controller that runs at 500 Hz, with policy inference at 50 Hz to derive the desired joint positions. Training occurs fully in simulation with moderate domain randomization, and the final control policy is deployed in a zero-shot manner without system identification or manual parameter adjustment. We conduct real-world experiments in a motion capture (Mocap) arena with a serving machine.

Beyond our EKF-based pipeline, we also explore a prediction-free variant that removes any explicit shuttle predictor. In contrast to recent humanoid table tennis systems where end-to-end RL is combined with an auxiliary learnable predictor that outputs hitting targets for a downstream controller [11], our variant does not introduce a separate prediction module. During training, the actor only receives the instantaneous shuttle pose plus five history pose frames to infer hit timing and target pose, while the critic retains privileged target to better learn the value function. This more tightly integrated end-to-end control strategy is conceptually closer to human-like rolling anticipation and may simplify deployment by avoiding additional predictor or planner tuning, but in this paper we only provide initial simulation evidence that the system can tolerate the absence of an explicit shuttle predictor. In the remainder of this work, we therefore focus on the EKF-based pipeline as our primary method, and report simulation-based comparisons to the prediction-free variant, leaving real-robot validation of this variant to future work.

Both simulation and real-world results indicate that our humanoid can execute large-amplitude swings while maintaining balance, react within sub-second windows, and intercept fast incoming shuttles fully autonomously without the aid of teleportation or motion demonstrations. While our current tests focus on machine-served shuttles in the Mocap arena, observed behaviors from the training recipe suggest a feasible path to higher-ceiling venues and, ultimately, rallies with robotic or human opponents. The key technical contributions are summarized as follows:

- First real-world humanoid badminton: an autonomous, unified whole-body controller that returns machine-served shuttles on a 21-DoF humanoid, achieving about 5.3 m/s swing speeds and producing outgoing shuttle speeds up to 19.1 m/s under sub-second reaction.
- Stage-wise RL for footwork–strike coordination: a three-stage curriculum that first establishes footwork, then introduces swing generation and precision striking, and finally removes locomotion-shaping regularizers to maximize hitting performance.
- A prediction-free variant: a more end-to-end policy that infers timing and hitting target implicitly from short-horizon shuttle observations, improving robustness to aerodynamic variability and removing explicit trajectory predictor.

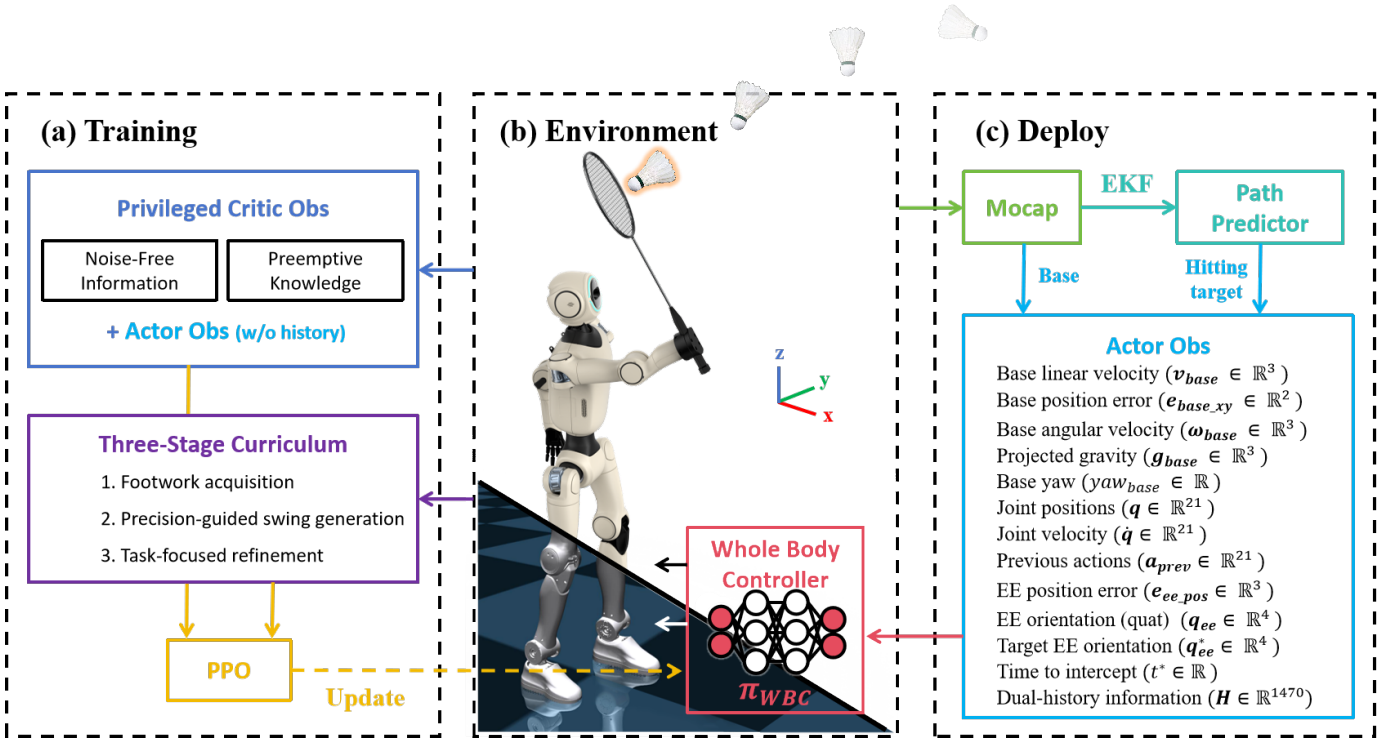


Fig. 2: **System overview.** (a) **Training:** PPO learns a single policy π_{WBC} using Privileged Critic Obs together with Actor Obs (no history) under a three-stage curriculum. All observations and rewards in (a) come from the simulation environment. (b) **Environment:** The humanoid is 1.28m tall, weighs 30kg, and has 21 DoF. A 3D-printed mount attaches the racket orthogonally to the forearm. The robot is initialized above the origin and faces the $+x$ direction. Shuttlecock position and base pose are obtained by motion capture using the marker. (c) **Deploy:** At runtime, Mocap directly provides the base state, while an EKF with a path predictor estimates the shuttle trajectory to produce the hitting target $\{p_{ee}^*, q_{ee}^*, t^*\}$. This information, together with proprioception and dual-history features, forms the complete Actor Obs. π_{WBC} consumes the Actor Obs and outputs whole-body actions executed by a low-level PD controller.

II. RELATED WORK

A. Whole-Body Loco-manipulation

Combining manipulation skills with flexible mobility is essential for a wide range of robotic applications. Typically, the base movement and end-effector tracking problems can be solved separately to reduce task complexity [13, 14, 15, 16]. The work in [13] proposes an MPC controller to track the desired end-effector position of an arm mounted on the quadruped with a standalone RL-based controller for locomotion. To catch objects in flight, [14] assigns the base movement, arm swing, and hand catching tasks to three policy modules. Similarly, [15] claims that decoupling upper-body and lower-body control into separate agents can achieve a more precise end-effector tracking performance when the robot is moving. Despite these promising advantages, there have been many efforts to unify lower and upper body control. Specifically, [17, 18, 19] leverage a multi-critic architecture to ease the optimization of coordinated behavior. Moreover, [20] introduces a physical feasibility reward design to guide the unified policy learning. As for recent works on dynamic whole-body tasks such as racket sports and tossing, performance hinges on coordinated whole-body impulse generation and timing, with

the legs contributing to power transmission rather than merely locomotion. Unified whole-body loco-manipulation has proved effective across these domains [12, 21, 22].

B. Robotic Racket Sports

The development of control strategies for robotic racket sports has become a key benchmark for assessing progress in whole-body loco-manipulation [10, 11, 12, 16, 23, 24]. The tight coupling between perception, target interception, and precise end-effector control makes these tasks particularly challenging. To achieve human-level table tennis, [8] proposes a highly modular and hierarchical policy architecture, combining learned components with carefully engineered modules. However, the resulting system is complex, requires significant manual design and tuning across modules, and relies heavily on real-world data collection. Building on this line of work, [10] and [11] both tackle humanoid table tennis. [10] demonstrates that a RL-based whole-body controller, together with a simple model-based planner for ball trajectory prediction and racket target planning, is sufficient for a humanoid robot to sustain rallies with a human opponent. Yet, this work depends on expert demonstrations to construct high-quality reference

motions. Meanwhile, [11] jointly trains an additional module during RL to predict ball trajectories and propose racket targets. In both cases, however, the base motion is executed by a separate command rather than emerging from a single unified goal, so lower-body footwork and upper-body striking are not jointly optimized by the policy. Moreover, [12] introduces a perception-informed whole-body policy for badminton on a quadrupedal platform, achieving impressive shuttlecock tracking and striking performance. However, the quadruped morphology substantially simplifies balance compared to a humanoid with a narrow support polygon and a high center of mass, making the coordination of balance and large-amplitude racket swings considerably less challenging. In this work, we instead focus on coordinated badminton skill learning on a humanoid platform. We train a single whole-body controller via a multi-stage reinforcement-learning curriculum, without expert demonstrations or a separate base command, and conduct a systematic evaluation of its performance in both simulation and real-world experiments.

III. SYSTEM OVERVIEW

Platform. The robot used in this work is a general-purpose humanoid Phybot C1 (1.28 m, 30 kg, 21 DoF), see Fig. 2(b). DoF distribution: each leg has 3 hip joints, 1 knee, 2 ankles; the torso has 1 waist; each arm has 3 shoulder joints and 1 elbow. All joints use cycloidal-reduction actuators. A standard 100 g full size badminton racket is rigidly clamped to the distal forearm by a 3D-printed mount, with the racket perpendicular to the forearm axis. Onboard sensing comprises an IMU and absolute encoders; we do not employ force or tactile sensors. Further hardware specifications are provided in the appendix.

Environment and frames. Experiments are conducted in a Mocap arena. The world frame is fixed to the court floor; to remain consistent with training, the robot is initialized nearly above the world origin and faces the positive x direction; z is upward. The mocap optical volume loses the shuttle above 2.8 m, so all serves are preferably constrained below this height.

Perception. A FZMotion motion capture system with 21 cameras provides measurements streamed over Wi-Fi to the robot. Markers are placed on the robot base, yielding base position, orientation, and linear velocity; the shuttle carries reflective tape on the tip and provides position only (insufficient features to instantiate a rigid body). Our nominal pipeline estimates shuttle state via an EKF and predicts interception by forward dynamics integration. A prediction-free variant bypasses forecasting and feeds only the current and a short history of shuttle positions to the policy.

Compute, control, and communications. All inference and control run on an Allspark-2 x86 platform with an Intel Core i7-1165G7. The onboard computer communicates with the motor control board via wired CAN (command path < 1 ms), and the control board drives all actuators on a CAN bus. Mocap data arrive over a Wi-Fi router, with typical delays of tens of milliseconds (about 1–2 policy cycles depending on link stability). Frequencies: mocap 210 Hz; policy 50 Hz; low-level PD controller 500 Hz. Per-joint PD gains and actuator

constants are listed in the appendix.

External devices and power. Serves are produced by a manually aimed ball machine with adjustable position and launching angle, up to 14 m/s shuttle speed. The robot is powered by a 72 V battery pack.

IV. LEARNING COORDINATED BADMINTON POLICY

A. RL-based Dynamic Whole-Body Controller

1) Multi-Stage Reinforcement Learning: We cast policy learning as a partially observable Markov Decision Process (MDP) $\mathcal{M} = (\mathcal{S}, \mathcal{O}, \mathcal{A}, \mathcal{P}, \mathcal{R})$. At time t , the (unobserved) state is $s_t \in \mathcal{S}$; the agent receives an observation $o_t \in \mathcal{O}$, applies action $a_t \in \mathcal{A}$, transitions with $s_{t+1} \sim \mathcal{P}(\cdot | s_t, a_t)$, and accrues reward $r_t = \mathcal{R}(s_t, a_t)$. We learn a parametric policy $\pi_\theta(a_t | o_t)$ that maximizes $J(\theta) = \mathbb{E}[\sum_t \gamma^t r_t]$.

Observation space. The actor’s basic observation is 87-D, concatenating proprioception information and external sensing from Mocap. On top of this 87-D vector, we stack short/long history of all joint positions, velocities, and actions (5 frames + 20 frames) [25], adding another 1470 features to mitigate partial observability (e.g., base-velocity noise). The critic observation has 98 dimensions in total, which include the privileged information used to enhance actor version observations, such as noise-free base and joint states as well as racket speed which may be difficult to acquire in the real world. Others are classified as preemptive knowledge used to make MDP well-posed for accurate value learning. All quantities are expressed in the world frame. Detailed information is listed in Fig. 2(a), (c).

Action space. The policy outputs 21 joint position targets for all DoF, scaled by a unified action scale of 0.25 and tracked by the low-level PD controller.

Episode Settings. Each episode contains six swing targets, following the configuration used by [12]. This design enables follow-through behavior learning but makes the value function depend on the number of hits remaining. We therefore adopt an asymmetric actor–critic [26], the critic receives additional preemptive information as mentioned above to stabilize value estimation, while the actor only uses deployable observations. Concretely, these are two subsequent hitting times, next target position and orientation, and the number of remaining targets.

Training Settings. We train with PPO [27] on a single Nvidia RTX 4090 using 4096 parallel environments in IsaacGym [28]. Both actor and critic are MLPs with hidden layers 512–256–128 and ELU activations. Other hyperparameters are reported in the appendix.

Three-stage curriculum. As shown in Fig. 2(a), we use a three-stage schedule with identical observation and action space across stages; only reward terms and their weights change. Training in each stage continues from the previous checkpoint once each stage’s primary objective has converged. The whole process throughout all stages takes 12.4 h wall-clock time on a single RTX 4090, after which the policy is ready for deployment.

- S1 — Footwork acquisition toward sampled hit regions: learn to approach target regions with reasonable lower

limb gait and maintain a stable, forward-facing posture while traversing between six sampled hit locations within an episode.

- S2 — Precision-guided swing generation: building on S1, introduce a sparse hit reward active only at the scheduled hit instant t^* to enforce timing. Start with loose pose accuracy to let a full swing emerge, then schedule tightening of position and orientation accuracy. Add light swing-style regularization for human-like kinematics, and strengthen energy, torque, and collision constraints for efficient, stable hits.
- S3 — Task-focused refinement: remove target approach reward (which is the main task reward in S1) and numerous gait-shaping regularization (e.g. foot distance, step/contact symmetry, step height) to avoid gradient interference with the hitting objective; keep safety, energy, and hardware limit constraint terms. Domain randomization and observation noise are enabled here to consolidate robustness.

We conduct a simple ablation study. Removing S1 and starting from S2 causes training to diverge directly. Skipping S2 and jumping directly from S1 to S3 makes the curriculum gap too large, and training again fails to reliably converge. Using S1–S2 yields a hardware-deployable policy but there’s still room for improvement. S3 breaks this plateau and improves performance and robustness.

2) *Multi-Stage Reward Design*: We devise a modular reward function that consists of a locomotion-style term r_{loco} and an arm hitting term r_{hit} to guide the emergence of coordinated badminton skills. The locomotion reward follows [29] and leverages feet swing-time to encode step frequency implicitly. While the hit reward references [12] but making some modifications. We group the remaining terms into global regularization r_{global} (action rate, joint limits, collision, energy etc.). Exact weights are reported in the appendix.

S1 — Footwork acquisition. Let $d = \|(p_{\text{ee}}^* - p_{\text{base}})_{xy}\|$. The main shaping encourages reaching the target region while not necessarily requiring precise approach, being nearby will suffice:

$$r_{\text{track}} = \exp(-4 \max(d - 0.3, 0)). \quad (1)$$

S1 applies standard style shaping for humanoid stable walking—base height and orientation, acceleration regularization, contact-aware footstep terms (air time, touchdown speed, step height, foot posture, no-double-flight), and simple gait symmetry shaping—plus face alignment to the incoming shuttle. Safety constraints (action rate, joint position/velocity/acceleration, torque, energy) follow legged_gym conventions [29]. With this shaping, S1 typically converges within 1k iterations, yielding reliable target-region tracking with natural gait.

S2 — Precision-guided swing generation. On top of S1, we lower the weight of regional tracking and introduce a hit-instant reward with large weight (six activations per episode). This reward comes with two terms, hitting precision and racket swinging speed. While [12] splits hitting precision into posi-

tion and orientation with different scales, we find it to be more accurate to entangle two terms together, coupling position and orientation accuracy [21]. Then we introduce another racket speed term to encourage swing. Define the target racket normal n^* as the z -axis of target hitting orientation q_{ee}^* . Let v_{ee} be the end-effector linear velocity; the effective speed component in the direction of target is $v_{\text{ee}} \cdot n^*$. Let $e_{\text{ee_pos}} = \|p_{\text{ee}} - p_{\text{ee}}^*\|$ and $e_{\text{ee_ori}} = \text{ang_err}_z(q_{\text{ee}}, q_{\text{ee}}^*)$ (defined as the angle between the current and target racket normals; only the normal direction is considered here, rewarding the full EE orientation would be possible but is not required for the hitting task). The hit reward, active only at $t = t_{\text{hit}}$, is

$$\begin{cases} r_{\text{swing}} = \exp\left(-\frac{e_{\text{ee_pos}}^2}{\sigma_p}\right) \exp\left(-\frac{e_{\text{ee_ori}}}{\sigma_r}\right) + 0.3 r_v, \\ r_v = 1 - \exp\left(-\frac{\max(0, v_{\text{ee}} \cdot n^*)}{\sigma_v}\right). \end{cases} \quad (2)$$

We start with wide pose tolerances $\sigma_p = 2.0$, $\sigma_r = 8.0$ to allow a full swing to emerge, and then schedule tightening of position and orientation accuracy to $\sigma_p = 0.1$, $\sigma_r = 1.0$ as training progresses. The racket speed sigma is fixed at $\sigma_v = 3.0$, so a 5 m/s swing yields $> 80\%$ of the speed term, balancing accuracy with deploy-time stability. We also add light swing-style regularization to align the racket short-edge (y) axis with the world y -axis,

$$r_{y\text{-align}} = (\hat{y}_{\text{ee}}^\top \hat{y}_{\text{world}})^2, \quad \hat{y}_{\text{ee}} = R(q_{\text{ee}}) \mathbf{e}_y, \quad (3)$$

which encourages the policy to adopt a more human-like hitting posture—performing a backswing and then swinging forward along the reverse of that backswing—to produce a more complete kinetic chain. We also reward a default holding pose when no shuttle is launched,

$$r_{\text{hold}} = - \sum_{j \in \mathcal{A}_{\text{arm}}} (q_j - q_j^{\text{hold}})^2, \quad (4)$$

where \mathcal{A}_{arm} denotes the set of arm joint indices. This improves deploy-time stability and recoverability. We also add collision penalties and strengthen energy, torque costs. In practice, policy first learns to bring the racket near the target and gradually develops an early backswing then swing with peak velocity near t^* ; with the scheduled tightening, after about 20k iterations, it progress to smooth backswing–swing–recovery with practical precision.

S3 — Task-focused refinement. Starting from the S2 checkpoint, we remove target approach reward and numerous gait-shaping terms in r_{loco} —foot distance, contact and step symmetry, step height—to avoid gradient conflict with the hitting objective. We retain global regularization terms and r_{hit} rewards, and enable domain randomization plus observation noise to consolidate robustness. With these enabled—thus making the environment deliberately harder—the policy does not regress; instead, we observe consistent improvements across metrics. The primary hitting reward r_{swing} increases by 3–5%, and we see lower action rates, reduced joint velocity and acceleration penalties, lower energy consumption, cleaner foot-contact force profiles, and reduced joint-torque usage; notably, the energy and torque costs decrease by $\approx 20\%$ empirically.

Global regularization (all stages). Action rate penalties, joint position/velocity/acceleration, torque limits follow standard legged gym practice; thresholds and weights are listed in the appendix.

B. Model-based Hitting Target Generation and Prediction

Building on the work presented in [12], we similarly adopted a model-based approach for both generating shuttlecock trajectories required for robot training and predicting hitting positions using physical models.

1) *Generate Shuttlecock Trajectory for Training:* To generate badminton flight trajectories for training purposes, we employ a physics-based simulation approach. This method adheres to the badminton dynamics model in [30], with the shuttlecock’s flight state updated according to the following equation:

$$m \frac{dv}{dt} = mg - m \frac{\|v\|v}{L} \quad (5)$$

where m represents the shuttlecock mass, v denotes its velocity, g is gravitational acceleration, and L is the aerodynamic characteristic length, defined as $L = 2m/\rho SC_D$. Here, ρ is air density, S is the cross-sectional area of the shuttlecock, and C_D is the drag coefficient. The computed aerodynamic length L used in our work is 3.4.

The generated shuttlecock flight trajectories were required to meet specific conditions to ensure data validity and relevance. To simulate realistic badminton hitting scenarios, we defined a hitting zone constrained by $x \in [-0.8, 0.8]$, $y \in [-1, 0.2]$, and $z \in [1.5, 1.6]$, with a minimum traversal time of 0.8 seconds. This filtering process effectively eliminated trajectories that did not conform to realistic hitting requirements, thereby ensuring the quality of the training data. Hitting zone in the y direction is asymmetric due to the right-hand racket setting.

Finally, the selected trajectories were combined with corresponding interception point data to construct a comprehensive training dataset containing position, orientation (trajectory tangential line as the racket normal), and timing features. These data are stored as tensors and can be directly utilized for subsequent training.

2) *Shuttlecock Trajectory Prediction for Deployment:* In the deployment phase, an EKF-based trajectory prediction algorithm was developed to achieve real-time shuttlecock flight estimation and hitting point prediction. This approach accounts for aerodynamic drag, gravitational acceleration, and sensor noise, providing accurate targets for the robot’s striking motion planning.

Our Extended Kalman Filter implementation adheres to the same badminton dynamics model as that used for shuttlecock trajectory generation. It operates through two distinct phases: measurement update and prediction. When the predicted height first falls into the predefined interception box, the spatial coordinates and time of traversal are designated as the predicted hitting target, expressed as: $\mathbf{p}_{ee}^* = [x_{hit}, y_{hit}, z_{target}]^T$ and t^* . The corresponding velocity vector at t_{hit} is then converted

into a quaternion representation to guide the robot’s end-effector orientation during the hitting motion. The prediction is activated at 0.36 s, once sufficient trajectory history has been collected, and then continuously updates the hitting target in a rolling manner, which is fed to the controller.

C. Prediction-free variant

We additionally train a prediction-free policy whose only change from the main pipeline lies in the observation space; the reward function, action space, training schedule (three-stage) remain identical. In this variant, the actor no longer receives the commanded hitting position, orientation, and time $(p_{ee}^*, q_{ee}^*, t^*)$. Instead, it ingests a sliding window of world-frame shuttle positions comprising the current frame and the previous five frames sampled at 50 Hz (i.e., $\{p_{sh}(t), p_{sh}(t-0.02), \dots, p_{sh}(t-0.10)\}$). From this short history the actor must implicitly infer the intended interception pose and timing. The critic retains privileged access to the “actual” interception point. This design is enabled by how training data are generated: for each commanded target, we not only sample the single interception point but also store the entire shuttle trajectory integrated by forward badminton dynamics. During training, the reward and the critic always know the ground-truth hit specification associated with the current shot, while the actor only observes the raw shuttle-history window.

A potential advantage of this variant is that deployment no longer relies on a hand-tuned predictor (e.g., an EKF plus a parametric aerodynamic model) to deliver $(p_{ee}^*, q_{ee}^*, t^*)$. Instead, the controller conditions directly on measured shuttle positions, making the overall pipeline more end-to-end and reducing explicit dependence on predictor or aerodynamic parameters. During training, we randomize aerodynamic parameters per shot, effectively exposing the policy to an “aerodynamic patch” whose exact coefficients need not be known. Intuitively, this mirrors human play: players do not know a specific shuttle’s drag constants a priori but infer landing tendencies from a brief flight segment. In simulation, the prediction-free policy achieves hitting performance with only a modest drop relative to the known-target setting, providing initial evidence that our system can cope without an explicit shuttle predictor. We do not evaluate potential deployment benefits of this variant on hardware, real-robot validation and a more thorough analysis of its robustness are left to future work.

V. EXPERIMENTS

We evaluate our approach with five experiments that together probe accuracy, agility, robustness, and deployability: (1) a simulation **Two-Robot Rally** that measures sustained rally length; (2) a simulation **Target-Known vs. Prediction-Free Comparison** that contrasts two observation designs under matched conditions; (3) an **EKF Prediction Accuracy** study that quantifies trajectory and intercept-point errors; (4) a real-world **Virtual-Target Swinging** test that assesses swing

speed and pose accuracy without a real shuttle; and (5) a **Real-World Shuttle Hitting** test that measures outgoing shuttle speed, reachable interception range, and return shot quality.

A. Experiment Settings

All simulation studies are performed in Isaac Gym and MuJoCo. Isaac Gym runs on a single RTX 4090; MuJoCo runs on CPU. During testing, a policy may hit any number of shuttles within an episode, not limited to six as training. For on-robot feasibility, we adopt a design target for “hit success” of position error below 0.10 m and orientation error below 0.2 rad at the scheduled impact time. This target is motivated by the racket geometry: 0.10 m is approximately the half-width of the racket’s short axis. In simulation, the controller’s ability to meet or exceed this target is what makes real-world hits possible later.

For simulation, the Two-Robot Rally uses a scaled singles court tailored to a 1.28 m humanoid: half-court length 4.0 m along x , half-court width 1.75 m along y , and a net height of 1.524 m. Unless otherwise noted, the aerodynamic model matches the one used to generate training trajectories. When evaluating the Prediction-Free policy we also vary the aerodynamic characteristic length within a bounded range to emulate different shuttles, while the Target-Known policy uses the fixed aerodynamics from training. For hardware deployment, the robot operates in a Mocap arena. The ball machine is placed at approximately $x = 5.2$ m from the origin. Interception heights are kept within 1.5–1.6 m to match training. The Virtual-Target Swinging test commands spatial targets without a shuttle to isolate swing behavior. The Ball-Machine Hitting test narrows the interception region for safety and field-of-view reasons and measures interception area and returns.

B. Simulation Results

1) *Two-Robot Rally*: Two identical humanoids stand on opposite sides of the scaled court, see Fig. 3 (a), both right-handed and both running the same Target-Known policy. The first interception target is sampled from the training-style distribution. After a side attempts a hit, we compute the outgoing shuttle velocity from the incoming shuttle state and the racket state at the contact instant, assuming a nearly elastic interaction with a racket inertia that dominates the shuttle. With racket-face normal n_{racket} , incoming velocity v_{incoming} , and racket velocity v_{racket} , we have:

$$\begin{cases} v_{\text{racket},n} = (v_{\text{racket}} \cdot n_{\text{racket}}) n_{\text{racket}}, \\ v_{\text{shuttle},n} = (v_{\text{incoming}} \cdot n_{\text{racket}}) n_{\text{racket}}, \\ v_{\text{out}} = v_{\text{incoming}} - 2v_{\text{shuttle},n} + 2v_{\text{racket},n}. \end{cases} \quad (6)$$

We then integrate the shuttle dynamics forward until it lands on the opposite half-court and alternate sides. The rally ends if a side falls, if the shuttle does not clear the net, if it lands out of bounds, or when the shuttle contacts the ground after a failed interception. Under this rule, we obtain rallies sustained to 21 consecutive returns, indicating that the controller can repeatedly reposition, return shuttle with high quality, and recover posture across extended exchanges.

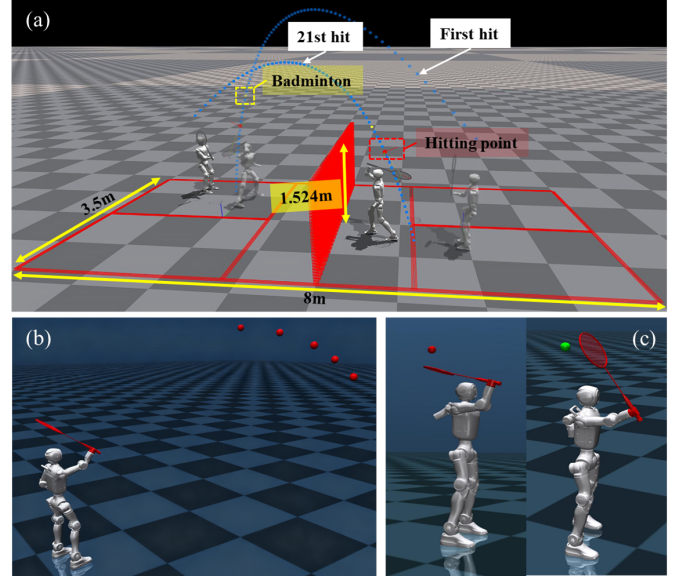


Fig. 3: **Simulation results.** Figure (a) illustrates the Two-Robot Rally scenario, where two identical humanoid robots sustain a rally of 21 consecutive returns. Figure (b) demonstrates the Prediction-Free policy: the robot infers the optimal impact position and orientation solely from the first five recorded shuttlecock positions after serving. Figure (c) presents the Target-Known policy, where a predetermined hitting position is provided. The red sphere indicates the designated hitting location, while the green sphere confirms successful impact execution by the robot.

2) *Target-Known vs. Prediction-Free Comparison*: This experiment contrasts two observation designs under identical scenes, robot initializations, and court geometry, as demonstrated in Fig. 3 (b) (c). The Target-Known policy receives the planned interception position, orientation, and time. The Prediction-Free policy instead observes the current shuttle position together with a five-frame history at 50 Hz and must infer the impact pose and timing from this short temporal window. All other components, including the reward design and training curriculum, are identical. The Target-Known evaluation uses the fixed aerodynamic parameters from training. The Prediction-Free evaluation samples moderate variations of the aerodynamic characteristic length to emulate different shuttles.

Each policy executes twenty hits sampled randomly. We report two quantities: the position and orientation errors at impact and the executed swing speed. As shown in Fig. 4, explicit target information is not indispensable: the policy can infer both the hitting target and the timing on its own with modest performance drop.

C. Sim2Real Transfer

We train the controller entirely in simulation and deploy to hardware in a zero-shot manner. To improve transfer, we apply domain randomization and observation noise during training; detailed ranges are provided in the appendix. We do

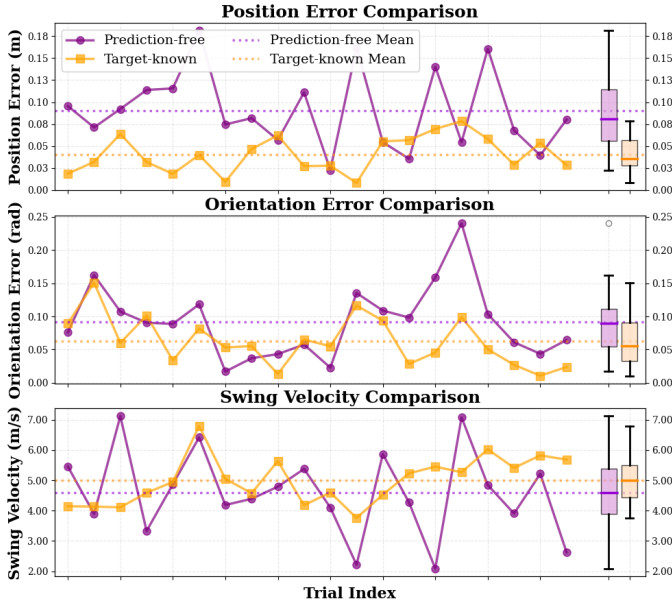


Fig. 4: Comparison between target-known and prediction-free policy. The top part of this figure shows the **position error** for both strategies. The middle section of the figure shows the **orientation error** comparison, the orientation corresponds to the normal direction of the racket face. The bottom part of the figure compares **swing velocity**.

not model additional delays, and we do not fit actuator network model [31] or conduct system identification [32]. Rotor inertias are computed from gear reduction. In practice, the learned controller carries over to the real robot in Mocap arena without special tricks, which we substantiate in the EKF Prediction Accuracy study and the two hardware experiments presented later.

D. Real Robot Deployment

In our real-world evaluation, we decompose the shuttlecock hitting task into two prerequisites, trajectory prediction and swing execution, followed by a final integrative test.

1) *EKF Prediction Accuracy study*: Prediction error refers to the deviation between the model’s predicted shuttlecock trajectory and the actual measured trajectory. Accurate trajectory prediction is critical for the robot to hit the shuttlecock at the right time and position. To quantify prediction errors, we collected 20 authentic badminton flight trajectories using a motion capture system. Partial segments of these trajectories were used as measurement input for the EKF. The EKF was then employed to generate predictions, which were subsequently compared against the ground-truth contact positions and timing. The comparative results are presented in Fig. 5. At 0.6 s before impact, the mean predicted position error falls below 100 mm, with the error bound sharply converging over time. By 0.3 s prior to contact, the mean position error has narrowed to 10 mm. Meanwhile, interception timing prediction achieves a mean error of approximately 20 ms at 0.6 s before hitting—already meeting task requirements—and

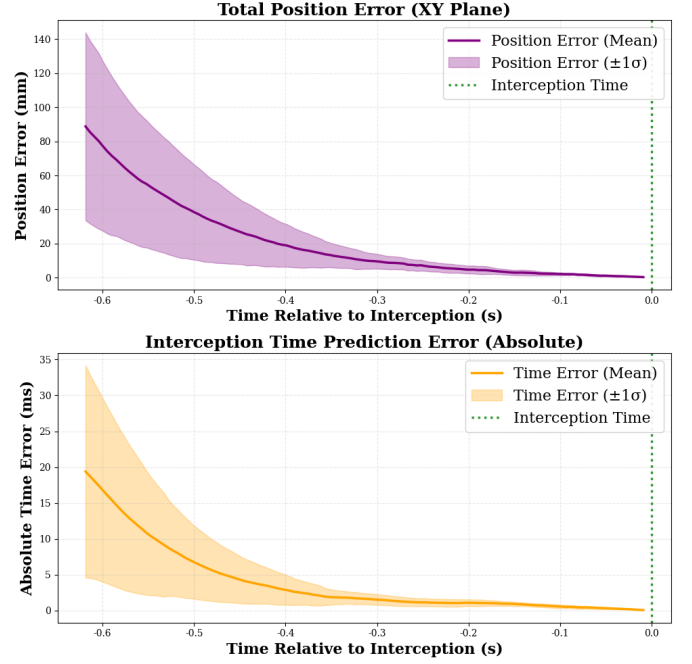


Fig. 5: **EKF Prediction Accuracy**. The predicted striking position error (top) and striking time error (bottom) were evaluated over 20 shuttlecock trajectories. The shaded regions represent the standard deviation. At 0.6 s before interception, the mean position error was less than 100 mm, already smaller than the radius of the racket.

similarly exhibits rapid convergence.

To evaluate the impact of prediction model parameter uncertainty on prediction performance, a characteristic length perturbation factor was randomly generated for each trajectory to reflect changes in aerodynamic parameters; specific results are provided in the appendix.

2) *Virtual-Target Swinging*: The racket swing error refers to the spatial deviation between the racket’s contact point with the shuttlecock and the sweet spot during execution. To quantify the robot swing error, a large number of randomly sampled target positions were designated, and Mocap was employed to measure the center position of the racket face. The robot was subsequently instructed to execute the hitting motion, and the actual measured interception point was compared against the commanded target position, the corresponding results are presented in Fig. 6.

We conducted a total of 71 virtual target swinging tests. The results show a mean Euclidean distance error of 24.29 mm with an average racket speed of 5.32 m/s at impact. These results verify that the robot can effectively control the contact point within the radius of the racket face during complex hitting tasks, confirming its practical feasibility for performing high-precision swinging actions.

3) *Real-World Shuttle Hitting*: When integrating two systems together in the real world, we set a ball machine to serve the shuttlecock and adjust its strength and pitch-yaw angles to test the capability of the policy. Because the shuttle’s relatively

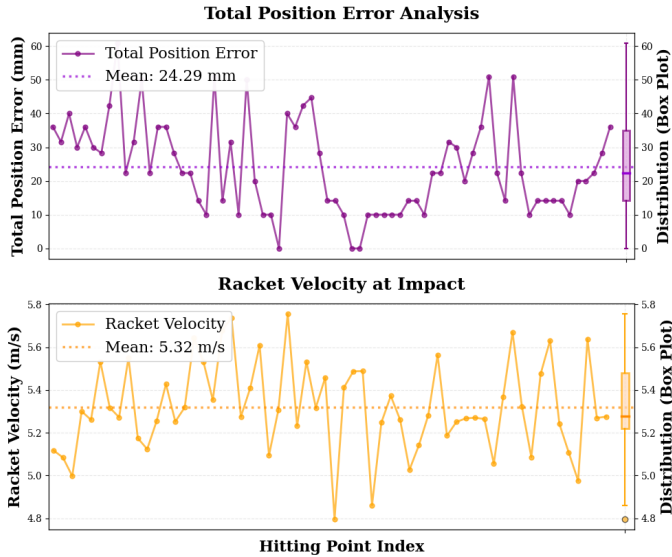


Fig. 6: **Virtual-Target Swinging.** The upper portion of the figure depicts the Euclidean distance error between the racket center and the designated hitting position at the moment of impact, while the lower portion illustrates the corresponding racket speed at impact.

flat trajectories in the indoor mocap environment leave only a very short reaction window, we constrain the interception area to a reasonable range for safety. We collect 46 hitting results; except for 4 shots that hits the edge of racket frame, the robot successfully returns all shuttles (success rate 91.3%) with coordinated and agile motion. As shown in Fig. 7, the robot intercepts the shuttlecock at about 1.4-1.7 m above the ground with the region of 98 cm x 50 cm. This is a relatively large area for a robot height only 1.28 m. We also observe that the robot not only manages to intercept the shuttle but also returns it with high quality, achieving outgoing shuttle speeds of up to 19.1 m/s, with an average of 11.1 m/s across trials, and producing sharp slope trajectories whose peak height exceeds 3 m, as shown in Fig. 1. Moreover, we measure the landing distance of the returned shots and obtain an average of about 4 m from the interception area, with only several outliers where the shuttle hits the ceiling or the racket frame.

VI. DISCUSSION

A. System Design

We train a single whole-body policy that coordinates stepping and striking rather than layering an arm controller on top of a lower-body controller. In badminton, hit quality depends on how the legs reposition and support the arm’s exertion while maintaining balance. The subtle movements of the lower limbs can effectively adjust the posture of the racket.

Our multi-stage curriculum proceeds in three clear steps: learn to reach interception regions with stable footwork; add a sparse, high-value hit signal so a full swing emerges and follow a sigma curriculum to improve accuracy with light style terms; finally remove a majority of lower-limb regularizers to

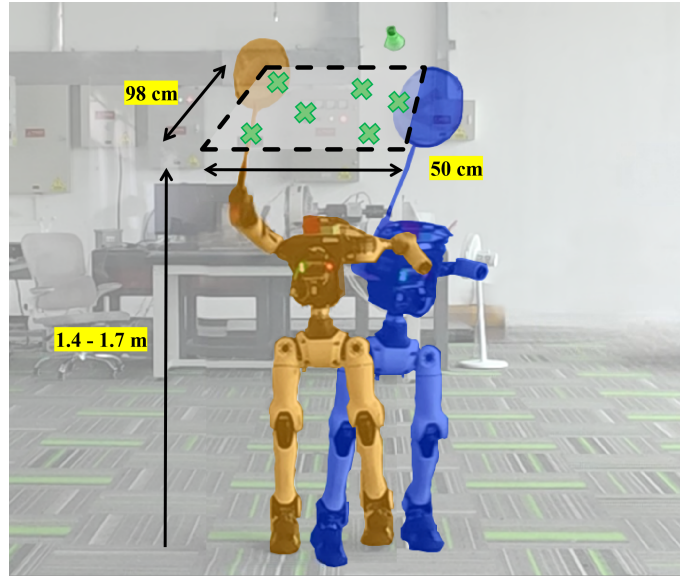


Fig. 7: **Real-World Shuttle Hitting.** This figure captures the robot’s actual hitting postures at the two opposing boundaries of the 98 cm x 50 cm interception area.

avoid gradients fighting the true objective of precise, energy-efficient hitting. During this stage, hitting metrics continue to improve while energy and torque costs drop, indicating progress toward task-optimal objective. Coupling position and orientation in the hit reward further prevents the policy from over-optimizing one at the expense of the other.

The controller develops two complementary coordination patterns. When the target is nearby or the time budget is sufficient, it takes short corrective steps and then commits to a backswing. When the target is far or the window is tight, it initiates a long stride while beginning the backswing in parallel. This foot–racket co-timing is not hand-coded; it emerges from the training. Several additional behaviors emerged without explicit incentives. At higher interception heights the policy sometimes produced brief “tiptoe” reaching, and between hits it recenters near the middle-right of the court, reflecting the sampled target distribution and matching human re-centering behavior.

Using six targets per episode teaches recovery and preparation between hits and reduces dependence on a particular initial posture. The asymmetric actor–critic design also matters: the critic receives preemptive knowledge that makes MDP well-posed and stabilizes value estimation, while the actor is restricted to deployable inputs.

Zero-shot transfer worked because domain randomization covered key dynamics and sensing variations, constraint terms discouraged brittle high-torque solutions, and the staged curriculum encouraged a complete kinetic chain for hitting rather than single-joint-dominant motion.

B. Limitations and Future Work

Dependence on the mocap arena with limited ceiling height constrains shuttle trajectories to low arcs driven by a ball

machine. During testing, shuttles occasionally hit the ceiling, and limited flight range makes long multi-ball rallies with human partners difficult. Higher ceilings and broader interception bands are expected to reveal more of the controller’s potential.

Moreover, the learned striking behavior remains relatively stereotyped. The current system predominantly discovers a single, forehand-like hitting style and does not yet exhibit the diverse repertoire of human strokes (e.g., backhand hits, lunges, jump and smashes), and the feasible interception area is restricted to a relatively narrow band.

Deploying the prediction-free variant on hardware remains future work. This variant removes explicit target prediction at deployment but relies on a strictly timed 50 Hz history of shuttle positions. Robust buffering and time-stamping will be needed so that the actor can infer velocities and timing from consistently spaced observations.

Moving toward pure vision would require reliable visual odometry and policies that keep the shuttle within the field of view during aggressive motion. A head-mounted camera that actively tracks the shuttle, together with learning signals that encourage aligning the view with the shuttle trajectory, appears to be a practical path to removing external tracking.

Above the low-level controller, a natural extension is to train a higher-level policy via multi-agent training to decide where to intercept, when to swing, and what racket-face orientation to command, and then invoke the whole-body controller as a motor primitive. Current failures arise when consecutive targets are too far apart for the available maneuver time; wider target sampling and reward shaping that explicitly encourages high-speed legged maneuvers are likely required to mitigate these cases.

Finally, the same framework may provide a path to adapt the pipeline to tennis or squash by replacing the shuttlecock dynamic “patch” and adjusting interception style, with modest reward retuning to reflect different sport-specific behaviors.

VII. CONCLUSIONS

In this work, we present the first real-world humanoid badminton system powered by a unified whole-body RL policy trained with a three-stage curriculum. The curriculum progresses from guiding lower-body footwork, to inducing a full swing and gradually tightening positional and orientation accuracy, and finally removing numerous gait regularizers to focus learning on precise, robust hitting. The policy produces human-like badminton behaviors that coordinate stepping and swinging under tight time windows, without any expert demonstrations.

In simulation, two identical humanoids sustain rallies with a best run of 21 consecutive returns, achieving a hitting accuracy within 0.10 m position error and 0.2 rad orientation error. A separate comparison shows that the prediction-free variant matches the behavior of its counterpart that uses known hitting targets, while remaining robust to moderate aerodynamic variation. On hardware, the controller achieves swing speeds of about 5.3 m/s and returns ball-machine serves with outgoing shuttle speeds up to 19.1 m/s under sub-second

timing, transferring zero-shot through domain randomization. We believe this framework marks an important step toward agile, interactive whole-body response tasks on humanoids. As next steps, we plan to deploy the prediction-free policy on hardware, move toward egocentric vision operation, and layer strategy learning via self-play so the robot can make its own hitting decisions.

REFERENCES

- [1] Ilija Radosavovic, Tete Xiao, Bike Zhang, Trevor Darrell, Jitendra Malik, and Koushil Sreenath. Real-world humanoid locomotion with reinforcement learning. *Science Robotics*, 9(89):eadi9579, 2024.
- [2] Takara E Truong, Qiayuan Liao, Xiaoyu Huang, Guy Tevet, C Karen Liu, and Koushil Sreenath. Beyondmimic: From motion tracking to versatile humanoid control via guided diffusion. *arXiv preprint arXiv:2508.08241*, 2(3), 2025.
- [3] Ri-Zhao Qiu, Shiqi Yang, Xuxin Cheng, Chaitanya Chawla, Jialong Li, Tairan He, Ge Yan, David J Yoon, Ryan Hoque, Lars Paulsen, et al. Humanoid policy~human policy. *arXiv preprint arXiv:2503.13441*, 2025.
- [4] Tairan He, Zhengyi Luo, Wenli Xiao, Chong Zhang, Kris Kitani, Changliu Liu, and Guanya Shi. Learning human-to-humanoid real-time whole-body teleoperation. In *2024 IEEE/RSJ International Conference on Intelligent Robots and Systems (IROS)*, pages 8944–8951. IEEE, 2024.
- [5] Xuxin Cheng, Yandong Ji, Junming Chen, Ruihan Yang, Ge Yang, and Xiaolong Wang. Expressive whole-body control for humanoid robots. *arXiv preprint arXiv:2402.16796*, 2024.
- [6] Ziwen Zhuang, Shenze Yao, and Hang Zhao. Humanoid parkour learning. *arXiv preprint arXiv:2406.10759*, 2024.
- [7] Tairan He, Wenli Xiao, Toru Lin, Zhengyi Luo, Zhenjia Xu, Zhenyu Jiang, Jan Kautz, Changliu Liu, Guanya Shi, Xiaolong Wang, et al. Hover: Versatile neural whole-body controller for humanoid robots. In *2025 IEEE International Conference on Robotics and Automation (ICRA)*, pages 9989–9996. IEEE, 2025.
- [8] David B D’Ambrosio, Saminda Abeyruwan, Laura Graesser, Atil Iscen, Heni Ben Amor, Alex Bewley, Barney J Reed, Krista Reymann, Leila Takayama, Yuval Tassa, et al. Achieving human level competitive robot table tennis. In *2025 IEEE International Conference on Robotics and Automation (ICRA)*, pages 74–82. IEEE, 2025.
- [9] David B D’Ambrosio, Navdeep Jaitly, Vikas Sindhwani, Ken Oslund, Peng Xu, Nevena Lazic, Anish Shankar, Tianli Ding, Jonathan Abelian, Erwin Coumans, et al. Robotic table tennis: A case study into a high speed learning system. In *Robotics: Science and Systems*, 2023.
- [10] Zhi Su, Bike Zhang, Nima Rahmanian, Yuman Gao, Qiayuan Liao, Caitlin Regan, Koushil Sreenath, and S Shankar Sastry. Hitter: A humanoid table tennis robot

- via hierarchical planning and learning. *arXiv preprint arXiv:2508.21043*, 2025.
- [11] Muqun Hu, Wenxi Chen, Wenjing Li, Falak Mandali, Zijian He, Renhong Zhang, Praveen Krisna, Katherine Christian, Leo Benaharon, Dizhi Ma, et al. Towards versatile humanoid table tennis: Unified reinforcement learning with prediction augmentation. *arXiv preprint arXiv:2509.21690*, 2025.
- [12] Yuntao Ma, Andrei Cramariuc, Farbod Farshidian, and Marco Hutter. Learning coordinated badminton skills for legged manipulators. *Science Robotics*, 10(102):eadu3922, 2025.
- [13] Yuntao Ma, Farbod Farshidian, Takahiro Miki, Joonho Lee, and Marco Hutter. Combining learning-based locomotion policy with model-based manipulation for legged mobile manipulators. *IEEE Robotics and Automation Letters*, 7(2):2377–2384, 2022.
- [14] Yuanhang Zhang, Tianhai Liang, Zhenyang Chen, Yanjie Ze, and Huazhe Xu. Catch it! learning to catch in flight with mobile dexterous hands. In *2025 IEEE International Conference on Robotics and Automation (ICRA)*, pages 14385–14391, 2025.
- [15] Yitang Li, Yuanhang Zhang, Wenli Xiao, Chaoyi Pan, Haoyang Weng, Guanqi He, Tairan He, and Guanya Shi. Learning gentle humanoid locomotion and end-effector stabilization control. *arXiv preprint arXiv:2505.24198*, 2025.
- [16] Haochen Wang, Zhiwei Shi, Chengxi Zhu, Yafei Qiao, Cheng Zhang, Fan Yang, Pengjie Ren, Lan Lu, and Dong Xuan. Integrating learning-based manipulation and physics-based locomotion for whole-body badminton robot control. *arXiv preprint arXiv:2504.17771*, 2025.
- [17] Zipeng Fu, Xuxin Cheng, and Deepak Pathak. Deep whole-body control: Learning a unified policy for manipulation and locomotion. In Karen Liu, Dana Kulic, and Jeff Ichnowski, editors, *Proceedings of The 6th Conference on Robot Learning*, volume 205 of *Proceedings of Machine Learning Research*, pages 138–149. PMLR, 14–18 Dec 2023.
- [18] Aravind Elanjimattathil Vijayan, Andrei Cramariuc, Mattia Risiglione, Christian Gehring, and Marco Hutter. Multi-critic learning for whole-body end-effector twist tracking. In Joseph Lim, Shuran Song, and Hae-Won Park, editors, *Proceedings of The 9th Conference on Robot Learning*, volume 305 of *Proceedings of Machine Learning Research*, pages 1470–1485. PMLR, 27–30 Sep 2025.
- [19] Zifan Wang, Yufei Jia, Lu Shi, Haoyu Wang, Haizhou Zhao, Xueyang Li, Jinni Zhou, Jun Ma, and Guyue Zhou. Arm-constrained curriculum learning for locomanipulation of a wheel-legged robot. In *2024 IEEE/RSJ International Conference on Intelligent Robots and Systems (IROS)*, pages 10770–10776. IEEE, 2024.
- [20] Dianying Hou, Chengrui Zhu, Zhen Zhang, Zhibin Li, Chuang Guo, and Yong Liu. Efficient learning of a unified policy for whole-body manipulation and locomotion skills. *arXiv preprint arXiv:2507.04229*, 2025.
- [21] Huy Ha, Yihuai Gao, Zipeng Fu, Jie Tan, and Shuran Song. Umi on legs: Making manipulation policies mobile with manipulation-centric whole-body controllers. *arXiv preprint arXiv:2407.10353*, 2024.
- [22] Yuntao Ma, Yang Liu, Kaixian Qu, and Marco Hutter. Learning accurate whole-body throwing with high-frequency residual policy and pullback tube acceleration. *arXiv preprint arXiv:2506.16986*, 2025.
- [23] Fan Yang, Zhiwei Shi, Sixian Ye, Jiazhong Qian, Wenjie Wang, and Dong Xuan. Varsm: Versatile autonomous racquet sports machine. In *2022 ACM/IEEE 13th International Conference on Cyber-Physical Systems (ICCPs)*, pages 203–214, 2022.
- [24] Zulfiqar Zaidi, Daniel Martin, Nathaniel Belles, Viacheslav Zakharov, Arjun Krishna, Kin Man Lee, Peter Wagstaff, Sumedh Naik, Matthew Sklar, Sugju Choi, et al. Athletic mobile manipulator system for robotic wheelchair tennis. *IEEE Robotics and Automation Letters*, 8(4):2245–2252, 2023.
- [25] Zhongyu Li, Xue Bin Peng, Pieter Abbeel, Sergey Levine, Glen Berseth, and Koushil Sreenath. Reinforcement learning for versatile, dynamic, and robust bipedal locomotion control. *The International Journal of Robotics Research*, 44(5):840–888, 2025.
- [26] Lerrel Pinto, Marcin Andrychowicz, Peter Welinder, Wojciech Zaremba, and Pieter Abbeel. Asymmetric actor critic for image-based robot learning. In *Proceedings of Robotics: Science and Systems*, Pittsburgh, Pennsylvania, June 2018.
- [27] John Schulman, Filip Wolski, Prafulla Dhariwal, Alec Radford, and Oleg Klimov. Proximal policy optimization algorithms. *arXiv preprint arXiv:1707.06347*, 2017.
- [28] Viktor Makoviychuk, Lukasz Wawrzyniak, Yunrong Guo, Michelle Lu, Kier Storey, Miles Macklin, David Hoeller, Nikita Rudin, Arthur Allshire, Ankur Handa, et al. Isaac gym: High performance gpu-based physics simulation for robot learning. *arXiv preprint arXiv:2108.10470*, 2021.
- [29] Nikita Rudin, David Hoeller, Philipp Reist, and Marco Hutter. Learning to walk in minutes using massively parallel deep reinforcement learning. In *Conference on robot learning*, pages 91–100. PMLR, 2022.
- [30] Caroline Cohen, Baptiste Darbois Texier, David Qu  r  , and Christophe Clanet. The physics of badminton. *New Journal of Physics*, 17(6):063001, 2015.
- [31] Jemin Hwangbo, Joonho Lee, Alexey Dosovitskiy, Dario Bellicoso, Vassilios Tsounis, Vladlen Koltun, and Marco Hutter. Learning agile and dynamic motor skills for legged robots. *Science Robotics*, 4(26):eaau5872, 2019.
- [32] Filip Bjelonic, Fabian Tischhauser, and Marco Hutter. Towards bridging the gap: Systematic sim-to-real transfer for diverse legged robots. *arXiv preprint arXiv:2509.06342*, 2025.

APPENDIX

A. System Parameters

Per-joint PD gains (Table I) list the proportional and derivative gains used by the 500 Hz joint-space PD controller for each controllable DoF in both simulation and deployment.

Actuator constants (Table II) summarize the four PhyArc actuator modules used on the robot, including physical size, reducer and gear ratio, nominal and no-load speeds (RPM), rated and peak torque (N·m), rated and peak power (W), and rotor inertia. These specifications are used to set torque/velocity limits, define dof properties, estimate power, and do safety checks in our experiments.

| stiffness (N·m/rad) | | damping (N·m/s/rad) | |
|---------------------|-----|---------------------|----|
| hip_pitch | 100 | hip_pitch | 10 |
| hip_roll | 100 | hip_roll | 10 |
| hip_yaw | 100 | hip_yaw | 10 |
| knee | 50 | knee | 10 |
| ankle_pitch | 50 | ankle_pitch | 5 |
| ankle_roll | 5 | ankle_roll | 5 |
| waist_yaw | 100 | waist_yaw | 10 |
| shoulder_pitch | 50 | shoulder_pitch | 10 |
| shoulder_roll | 50 | shoulder_roll | 10 |
| shoulder_yaw | 5 | shoulder_yaw | 5 |
| elbow_pitch | 50 | elbow_pitch | 10 |

TABLE I: Per-joint PD gains

| Actuator model (PhyArc series) | 47 | 68 | 78 | 102 |
|--------------------------------|---------|---------|---------|-----------|
| Size | Ø47×68 | Ø68×75 | Ø78×79 | Ø102×54.8 |
| Reducer type | Cycloid | Cycloid | Cycloid | Cycloid |
| Reduction ratio | 25 | 25 | 25 | 25 |
| Rated speed (RPM) | 100 | 100 | 100 | 100 |
| Rated torque (N·m) | 3 | 28 | 40 | 60 |
| No-load speed (RPM) | 343.8 | 181.5 | 120 | 124.2 |
| Rated power (W) | 216 | 720 | 720 | 1080 |
| Peak power (W) | 864 | 4608 | 4608 | 5760 |
| Peak torque (N·m) | 12 | 96 | 136 | 244 |
| Rotor inertia | 0.00719 | 0.0339 | 0.0634 | 0.1734 |

TABLE II: Actuator constants

B. Training Details

Hyperparameters (Table III) define the PPO and training configuration used in our experiments. **Domain randomization and observation noise** (Table IV) specify the environment perturbations and sensor-noise settings applied during training. **Reward weights by stage** (Table V) records the curriculum’s stage-wise weighting of r_{loco} , r_{hit} , and r_{global} . Together, these tables precisely describe the training setup and support reproducibility.

| Hyperparameter | Setting |
|--------------------|-----------------|
| discount factor | 0.99 |
| GAE lambda | 0.95 |
| learning rate | adaptive |
| KLD target | 0.01 |
| clip param | 0.2 |
| control dt (s) | 0.02 |
| num. envs | 4096 |
| actor MLP size | (512, 256, 128) |
| critic MLP size | (512, 256, 128) |
| network activation | elu |
| optimizer | AdamW |

TABLE III: Hyperparameter configuration

| Domain random | Range | Noise | Range |
|----------------------|---------------|---------|-------|
| friction range | [0.5, 1.0] | dof_pos | 0.05 |
| push interval | 5 | dof_vel | 0.2 |
| max push vel_xy | 0.5 | lin_vel | 0.2 |
| max push ang_vel | 0.5 | ang_vel | 0.1 |
| added base_com range | [-0.08, 0.08] | gravity | 0.1 |
| join_friction range | [0.01, 1.0] | | |
| added inertia range | [0.01, 0.1] | | |

TABLE IV: Domain randomization and observation noise

TABLE V: Reward weights by stage

| Stage | Category | Term | Weight |
|-----------|---------------------|----------------------|---------------------|
| S1 | | | |
| S1 | r_{loco} | base_height | 5 |
| S1 | r_{loco} | base_ang_vel_xy | -10 |
| S1 | r_{loco} | base_orientation | -50 |
| S1 | r_{loco} | contact_no_vel | -10 |
| S1 | r_{loco} | feet_orientation | 10 |
| S1 | r_{loco} | feet_no_fly | -2 |
| S1 | r_{loco} | feet_height | 10 |
| S1 | r_{loco} | feet_distance | 2 |
| S1 | r_{loco} | air_time & land_time | -500 |
| S1 | r_{loco} | sym_contact_forces | 1 |
| S1 | r_{loco} | sym_step | -5 |
| S1 | r_{loco} | face_the_net | 8 |
| S1 | r_{loco} | target_approach | 30 |
| S1 | r_{hit} | — | — |
| S1 | r_{global} | action_rate | -0.8 |
| S1 | r_{global} | dof_pos_limit | -30 |
| S1 | r_{global} | dof_vel_limit | -0.1 |
| S1 | r_{global} | dof_torque_limit | -0.1 |
| S1 | r_{global} | dof_acc | -5×10^{-5} |
| S1 | r_{global} | dof_vel | -1×10^{-3} |
| S1 | r_{global} | dof_torque | -1×10^{-4} |
| S1 | r_{global} | momentum_positive | 5 |
| S2 | | | |
| S2 | r_{loco} | base_height | 5 |
| S2 | r_{loco} | base_ang_vel_xy | -10 |
| S2 | r_{loco} | base_orientation | -50 |
| S2 | r_{loco} | contact_no_vel | -10 |
| S2 | r_{loco} | feet_orientation | 10 |
| S2 | r_{loco} | feet_no_fly | -2 |
| S2 | r_{loco} | feet_height | 10 |
| S2 | r_{loco} | feet_distance | 2 |
| S2 | r_{loco} | air_time & land_time | -500 |

| Stage | Category | Term | Weight |
|-----------|---------------------|----------------------|---------------------|
| S2 | r_{loco} | sym_contact_forces | 1 |
| S2 | r_{loco} | sym_step | -5 |
| S2 | r_{loco} | face_the_net | 5 |
| S2 | r_{loco} | target_approach | 15 |
| S2 | r_{hit} | r_{swing} | 4000 |
| S2 | r_{hit} | $r_{y\text{-align}}$ | 5 |
| S2 | r_{hit} | r_{hold} | 10 |
| S2 | r_{global} | action_rate | -0.8 |
| S2 | r_{global} | dof_pos_limit | -30 |
| S2 | r_{global} | dof_vel_limit | -0.1 |
| S2 | r_{global} | dof_torque_limit | -0.1 |
| S2 | r_{global} | dof_acc | -5×10^{-5} |
| S2 | r_{global} | dof_vel | -1×10^{-3} |
| S2 | r_{global} | dof_torque | -1×10^{-4} |
| S2 | r_{global} | momentum_positive | 5 |
| S2 | r_{global} | energy | -0.01 |
| S2 | r_{global} | collision | -10 |
| S3 | | | |
| S3 | r_{loco} | base_height | 5 |
| S3 | r_{loco} | base_ang_vel_xy | -10 |
| S3 | r_{loco} | base_orientation | -50 |
| S3 | r_{loco} | contact_no_vel | -10 |
| S3 | r_{loco} | feet_orientation | 10 |
| S2 | r_{loco} | feet_no_fly | -2 |
| S3 | r_{loco} | air_time & land_time | -500 |
| S3 | r_{loco} | face_the_net | 5 |
| S3 | r_{hit} | r_{swing} | 4000 |
| S3 | r_{hit} | $r_{y\text{-align}}$ | 5 |
| S3 | r_{hit} | r_{hold} | 10 |
| S3 | r_{global} | action_rate | -0.8 |
| S3 | r_{global} | dof_pos_limit | -30 |
| S3 | r_{global} | dof_vel_limit | -0.1 |
| S3 | r_{global} | dof_torque_limit | -0.5 |
| S3 | r_{global} | dof_acc | -5×10^{-5} |
| S3 | r_{global} | dof_vel | -1×10^{-3} |
| S3 | r_{global} | dof_torque | -1×10^{-4} |
| S3 | r_{global} | momentum_positive | 5 |
| S3 | r_{global} | energy | -0.01 |
| S3 | r_{global} | collision | -10 |

C. Supplementary Explanation for Model-based Hitting Target Generation

During trajectory generation, we employed a fixed time step for each trajectory and updated the shuttlecock's position and velocity through numerical integration. The initial positions and velocities were randomly generated within specified ranges to ensure diversity in the training data, with detailed settings in (7) [12]:

$$\begin{cases} p_{x,t_0} \sim U(5, 8) \\ p_{y,t_0} \sim U(-2, 2) \\ p_{z,t_0} \sim U(-0.5, 2.5) \\ v_{x,t_0} \sim U(-25, -13) \\ v_{y,t_0} \sim U(-3, 3) \\ v_{z,t_0} \sim U(9, 18) \end{cases} \quad (7)$$

This study develops a shuttlecock trajectory generator based on aerodynamic principles, employing numerical integration to simulate flight trajectories and filtering them according to predefined hitting criteria for robot training purposes, as

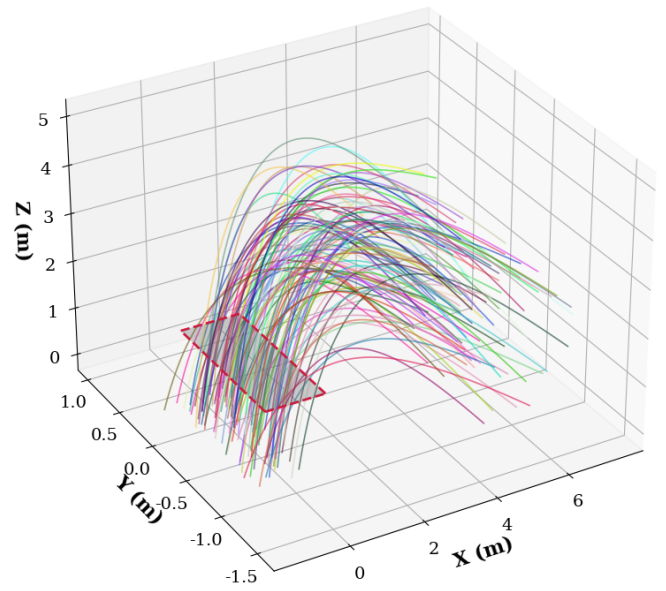


Fig. 8: **Trajectory generation.** Shuttlecock trajectories are filtered to ensure interception points within the region $x \in [-0.8, 0.8]$ m, $y \in [-1, 0.2]$ m and $z \in [1.5, 1.6]$ m for robot training.

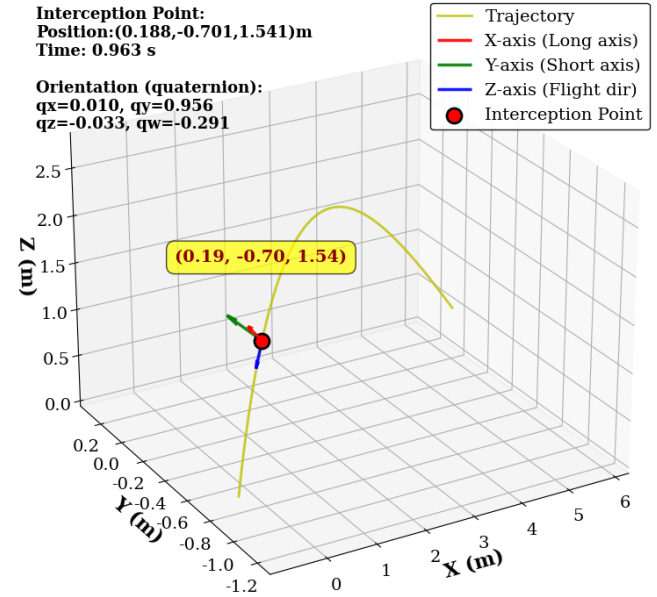


Fig. 9: **Individual trajectory analysis.** An example of sampled shuttle flight trajectory (gold) with the selected interception point (red). Corresponding target frame at the intercept is drawn, where z is the incoming-flight direction. The annotation reports the intercept position, orientation and time-to-intercept.

illustrated in Fig. 8. The specific characteristics of a single trajectory are examined in Fig. 9.

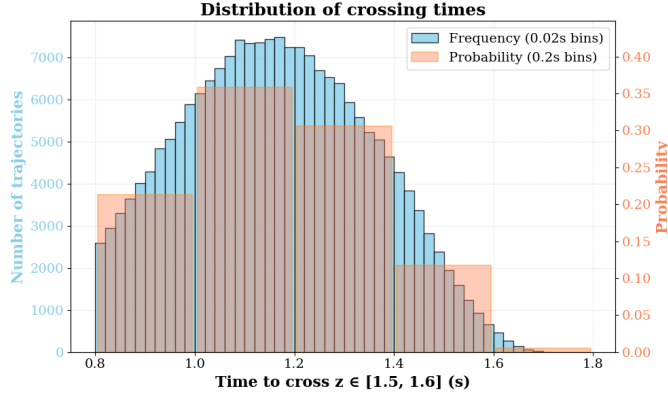


Fig. 10: **Training trajectory statistics.** Distribution of the shuttlecock interception time.

We generated 2 million trajectories, from which 196,940 met the criteria and were selected for robot training. The majority of these trajectories reached the hitting zone within a time interval of $[0.8, 1.4]$ seconds, as shown in Fig. 10.

D. Sensitivity Analysis of Prediction Parameters

For the 20 real-world badminton trajectories collected in our experiments, we perform a simple sensitivity analysis with respect to the aerodynamic characteristic length L . For each trajectory, we randomly sample a multiplicative perturbation factor $\alpha \sim \mathcal{U}(0.8, 1.2)$ and set the effective characteristic length to $L' = \alpha L$. We then recompute the shuttle predictions under these perturbed parameters, and summarize the resulting errors in Fig. 11. Although the perturbation degrades prediction accuracy, the mean position error still converges to within 10 cm by about 0.45 s before interception.

E. Repeatability Accuracy of Swing

During the real-world Virtual-Target Swinging test, we assessed repeatability precision by commanding a single fixed interception target and executing 20 independent swings. The racket center was tracked in real time using a motion-capture system. At the designated hit instant, positional error was defined as the distance between the captured racket-center coordinate and the target position. The resulting 3D trajectories of the racket center across the 20 trials are presented in Fig. 12, while Fig. 13 visualizes the distance between the racket center and the target position over 20 repeated swings.

F. Striking Motion Analysis

The complete real-world striking sequence for a representative return is illustrated in Fig. 14. When no shuttle is coming, the robot keeps stepping in place with the racket held in front of the body. Once a shuttle is launched, the controller initiates approach step(s) while simultaneously performing a backswing. During the hitting instant, the legs and arm accelerate in a coordinated manner to generate a whole-body impulse and produce a high racket speed. Notably, the non-racket arm swings in the opposite direction during the fast stroke, which helps counteract overall angular momentum and

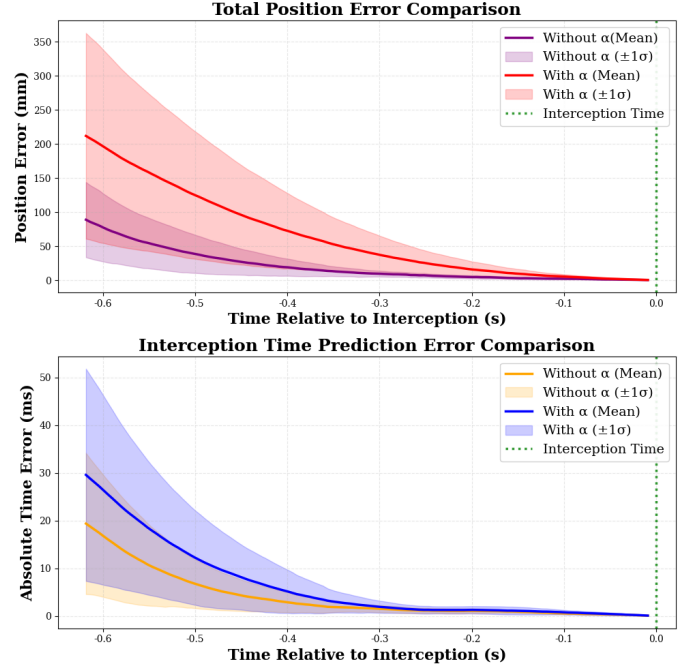


Fig. 11: **EKF prediction accuracy under varying aerodynamic characteristic lengths.** The parameter α scales the characteristic length to emulate variations in shuttle aerodynamics.

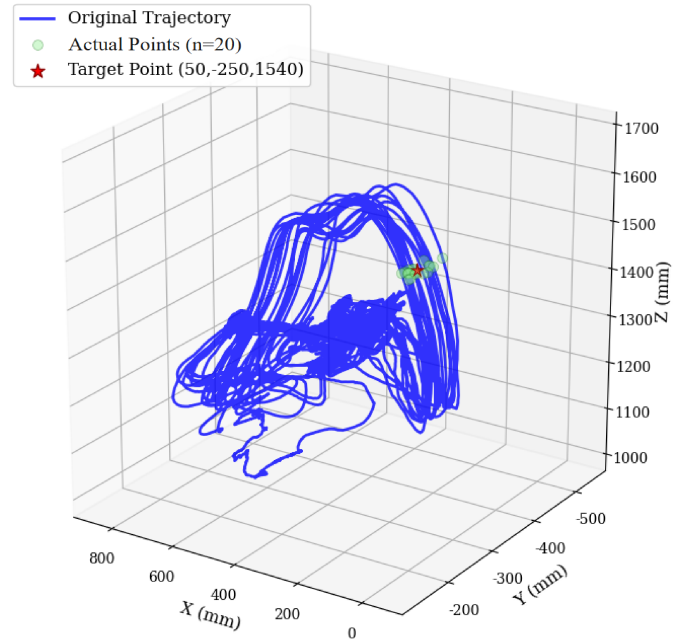


Fig. 12: **Trajectory of the racket center.** For a designated hitting position at $(50, -250, 1540)$ mm, the robot executed 20 swinging motions. The green spheres represent the positions of the racket center as it passed through the $z = 1540$ mm plane during each swing.

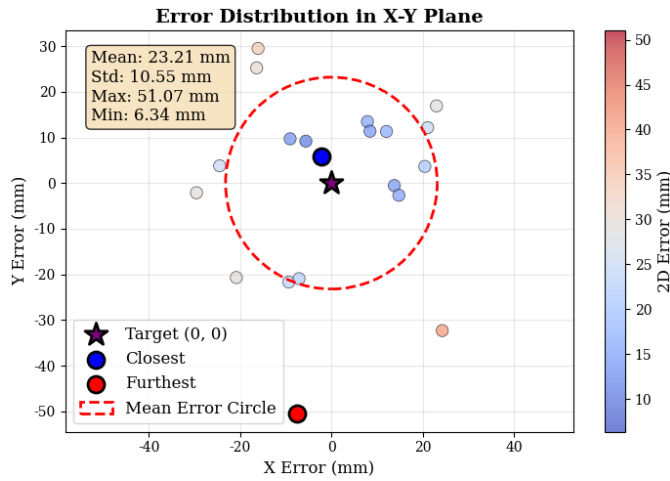


Fig. 13: **Swing Error Analysis.** Over 20 repeated swings, the mean Euclidean distance error was measured at 23.21 mm, with a standard deviation of 10.55 mm. The maximum and minimum errors recorded were 51.07 mm and 6.34 mm, respectively.

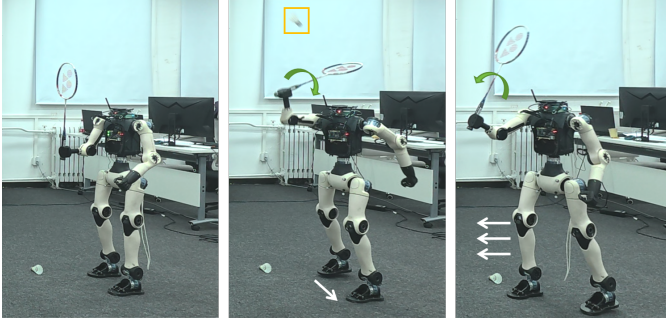


Fig. 14: **Real-world striking motion.** Three snapshots of a successful return in the real world. **Left:** in-place stepping before the shuttle is launched. **Middle:** approach and back-swing phase as the shuttle launched (yellow box highlights the shuttle, the green arrow indicates the racket swing direction, and the white arrow indicates the stepping motion). **Right:** hit and follow-through: the robot simultaneously takes a step and swings the racket toward the shuttle, then completes the motion with a follow-through.

maintain balance. After striking, the robot performs a recovery motion.